

# Phase-resolved imaging of coherent phonon-magnon coupling

Yannik Kunz,<sup>1,\*</sup> Florian Kraft,<sup>1</sup> David Breitbach,<sup>1</sup> Torben Pfeifer,<sup>2</sup>  
Matthias Kieß,<sup>3</sup> Stephan Glamsch,<sup>3</sup> Manfred Albrecht,<sup>3</sup> and Mathias Weiler<sup>1</sup>

<sup>1</sup>*Fachbereich Physik and Landesforschungszentrum OPTIMAS,*

*Rheinland-Pfälzische Technische Universität Kaiserslautern-Landau, 67663 Kaiserslautern, Germany*

<sup>2</sup>*Zernike Institute for Advanced Materials, University of Groningen, Groningen 9747 AG, The Netherlands*

<sup>3</sup>*Institute of Physics, University of Augsburg, 86135 Augsburg, Germany*

(Dated: March 9, 2026)

We use a direct phase-resolved optical technique to study the coherence of spin waves (SWs) that are driven by surface acoustic waves (SAWs) via resonant magnetoelastic coupling. For this, we employ a piezoelectric lithium tantalate (LiTaO<sub>3</sub>) substrate, equipped with micropatterned interdigital transducers for SAW excitation, which interact with SWs in a 5 nm thin and 20 μm wide Co<sub>40</sub>Fe<sub>40</sub>B<sub>20</sub>-waveguide. We detect the SAW and the SW using a phase-locked micro-focused optical polarization detection experiment and use the characteristic polarization dependence to separate the SAW and SW signals. Our measurements directly image the resonant and coherent excitation of the SW by the SAW.

Keywords: Magnonics, Magnetoelastics, Phonon-Magnon-interactions

*Introduction.* As nanoscale electronic circuits are reaching their physical limitations [1], Spintronics provides a complementary approach for information transport and processing as spin currents convey the information by transportation of spin angular momentum [2–4]. This spin transport does not necessarily require a charge current [5], as the spin information can be transported by excitations of the magnetic order parameter, consequently bypassing the resistive energy loss to Joule heating [6]. Spin currents can be generated by for instance the spin-Seebeck effect [7] or spin-pumping [8–10]. The specialized field of magnonics [11] explicitly makes use of coherent spin currents in the form of spin waves (SWs). SWs with their quanta, the magnon, are the low energetic excitations of magnetically ordered systems, locally deflecting the magnetization from its equilibrium. The applications of coherent SWs range from signal processing [12] to quantum computing [13, 14] and neuromorphic computing [15, 16]. Especially for the latter, magnons are promising candidates due to their intrinsic non-linearity that is accessible at low powers [17–19].

A key challenge for magnonics is that, although the SWs operate in a low-energy, low-dissipation regime, the coherent excitation by microwave antennas is rather inefficient, due to their weak coupling to microwave electronic circuits [20]. An approach to circumvent this is to exploit surface acoustic waves (SAWs), that couple via magnetoelastic interaction to the spin domain. The magnetoelastic mechanism for acoustic excitation of spin dynamics was already proposed by Kittel [21] and experimentally established shortly thereafter [22]. Previous studies showed that SAWs can be used to efficiently excite SWs linearly [23], parametrically [24] and non-linearly [25], even in ultra-low magnetic damping materials [26, 27], with the magnon-phonon interaction reaching

the limit of strong coupling [28, 29].

A key necessity for magnonic devices that operate with SAW driven SWs is to retain a well-defined phase relation between the microwave, the SAW and the SW. For this, it is required to directly demonstrate that the SWs driven by the SAW are indeed coherent. Typical experiments employing electrical detection commonly only probe the absorption of the SAW in transmission experiments due to the SW excitation [30–32]. These experiments do not provide evidence of the degree of coherence of the generated SWs, but only probe the SAW dissipation. Contrary, micro-optical experiments are a powerful tool for expanding research on phonon and magnon dynamics by providing space-, time-, and frequency-resolution [33–35]. Our previous micro-focused Brillouin-light-scattering (μBLS) experiments provided evidence that the magnon-signal is coherent to the SAW signal by evaluating the interference of light scattered by SAWs and SWs [36]. However, it is an open task to reveal the phase relationship between SAW and SW directly during resonant magnetoacoustic interaction, depending on space and the magnetic field.

Here, we present the direct imaging of resonant, coherently driven SWs by shear-horizontal SAWs (SH-SAWs). We achieve this by employing micro-focussed frequency-resolved polar-magneto-optical Kerr-effect (MOKE) based spectroscopy, termed the  $\mu FR$ -MOKE technique [37], an established technique alongside μBLS, that provides phase resolution similar to phase-resolved μBLS [38, 39] or micro-focused super-Nyquist sampling MOKE [18]. Advantageously, as  $\mu FR$ -MOKE is based on vector-network analysis it can operate in a wider frequency range compared to phase-resolved μBLS and does not require the synchronization of pulsed lasers and electronics that is necessary for micro-focused super-Nyquist sampling MOKE. We introduce a concept to separate SAW-generated signals from SW signature and show the intensity and phase modulation of the

\* ykunz@rptu.de

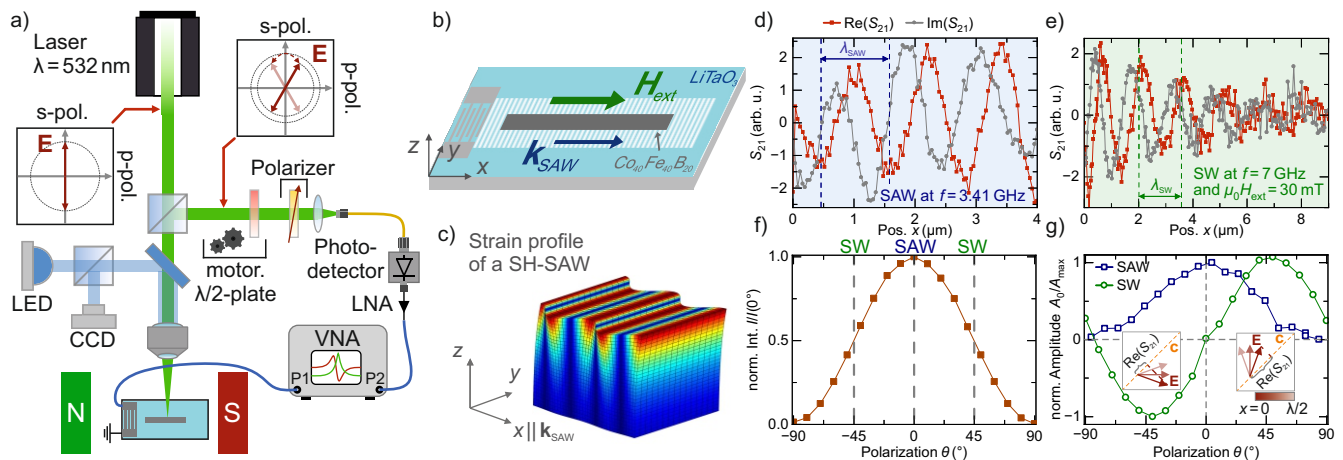


FIG. 1. (a) Schematic depiction of the experimental setup employing phase-locked micro-focused optical polarization analysis, commonly referred to as the  $\mu$ FR-MOKE-technique. The reflected laser light is analyzed in its polarization and intensity state at fixed temporal wave phase  $\omega t = \text{const.}$  (b) A sketch of the investigated sample: On a  $\text{LiTaO}_3$ -piezoelectric substrate, sets of IDTs excite coherent SH-SAWs toward a 5 nm thick and 20  $\mu\text{m}$  wide  $\text{Co}_{40}\text{Fe}_{40}\text{B}_{20}$ -waveguide. (c) The in-plane-polarized shear-strain profile of the propagating SH-SAW mode. The strain amplitude of  $\varepsilon_{xy}$  is shown in false color. (d) Example line-scan measurement of a SH-SAW mode on  $\text{LiTaO}_3$ , measured at  $f = 3.41$  GHz. The real and imaginary part of the  $S_{21}$  parameter, measured by the VNA, encode the phase-information of the detected SAW. (e) Line-scan measurement of a spin wave on a 40 nm thick permalloy film, excited by a microwave antenna, measured at  $f = 7$  GHz and  $\mu_0 H_{\text{ext}} = 30$  mT in Damon-Eshbach geometry ( $k_{\text{SW}} \perp \mu_0 H_{\text{ext}}$ ). (f) The light intensity as a function of the polarization, analyzed by the rotatable  $\lambda/2$ -plate measured after the polarizer, relative to the incoming polarization on the sample. The incoming, unmodulated light is linearly p-polarized. (g) Polarization dependence of the detected amplitude of the real-part of the SH-SAW and SW-signals, respectively. Notably, the SAW signal maximizes at highest sensitivity on intensity modulation and not undergoing a sign change from negative to positive polarization analysis, showing an even symmetry. Comparably, the SW is detected most efficiently at polarization modulating sensitivity and exhibiting a sign change from negative to positive polarization analyzing angle, representing an odd symmetry. The inset illustrates the origin of the sign flip of the SW detection, which occurs when the polarization is rotated due to a different selection of the analyzed polarization orientation.

SAW. Finally, we directly demonstrate the resonant and coherent driving of SW precession by the SAW.

*Experimental Methods* To spatially resolve the magnetoelastic interaction, we use the experimental setup schematically shown in Fig. 1 a), based on the  $\mu$ FR-MOKE-technique [37]. Hereby, we use a linearly polarized  $\lambda_1 = 532$  nm continuous wave laser that is focused on the sample using a 100x/0.75 NA microscope objective with a refraction limited spot size of approx.  $d_{\text{spot}} = \lambda_1/(2NA) \approx 355$  nm. The light interacts with the coherently excited acoustic or spin wave and is thereby modulated in polarization and intensity, depending on the probed spatial wave phase. The reflected light is coupled out using a beam splitter and passes a polarization analyzer unit consisting of a rotatable  $\lambda/2$ -plate and a polarizer, converting the polarization modulation into an intensity modulation. This intensity modulation is captured by a fast broadband photodetector via an optical fiber. The photodetector's output passes through a low-noise amplifier and is connected to port 2 of a vector network analyzer (VNA). Port 1 of the VNA is used as a microwave output to excite the acoustic or spin wave on the sample. With the phase-resolving ability of the VNA we measure the complex-valued  $S_{21}$ -transmission parameter that is directly sensitive to the probed wave

phase:

$$S_{21} = \frac{V_2}{V_1} \propto m_{\text{oop}} \cdot \exp(ik_{\text{SW}}x); \varepsilon_{ij} \cdot \exp(ik_{\text{SAW}}x), \quad (1)$$

$$S_{21}, m_{\text{oop}}, \varepsilon_{ij} \in \mathbb{C}.$$

Here,  $V_{1,2}$  are the voltages at the output port 1 and detection port 2 of the VNA,  $m_{\text{oop}}$  is the dynamic out-of-plane magnetization component  $m_{\text{oop}} = M_{\text{oop}}/M_S$  and  $\varepsilon_{ij}$  is the strain of the acoustic wave mode. The spatial resolution is realized by a Köhler illumination and a CCD-camera that is coupled in and out of the light path by a dichroic mirror.

For SAW generation, we use piezoelectric  $\text{LiTaO}_3$  as a substrate and sets of interdigital transducers (ITDs), as shown in Fig 1 b). Details on the sample fabrication are found in the supplemental material [40]. Importantly, the  $\text{LiTaO}_3$  supports the excitation of a shear-horizontal SAW mode, which is an in-plane polarized shear wave with a dominant  $\varepsilon_{xy}$  strain component that decays exponentially into the material along the  $-z$ -direction, as depicted in Fig. 1 c). The result of an exemplary line scan measurement at a frequency of  $f = 3.41$  GHz using a microwave power of  $P_{\text{MW}} = 12$  dBm is shown in Fig. 1 d), clearly demonstrating the spatially resolved wave fronts of the propagating SAW in  $\text{Re}(S_{21})$  and

$\text{Im}(S_{21})$ . The detection mechanism relies on the elasto-optic effect, in literature also referred to as photoelastic, acoustooptic or Pockels-effect, and is explained by a modulation of the reflectivity and induced birefringence [41–45], which depends on the strain profile of the acoustic mode. The SAW can interact with the SWs in a 5 nm thick and 20  $\mu\text{m}$  wide  $\text{Co}_{40}\text{Fe}_{40}\text{B}_{20}$  waveguide. Separately, we analyze the detection characteristics of SWs using a 40 nm thick film of permalloy with a microwave antenna for direct SW excitation. A typical measurement result is depicted in Fig. 1 e), revealing the SWs wavelength and decay length  $\xi$  by its envelope. Here, we employed the Damon-Eshbach geometry, meaning the wave vector  $k_{\text{SW}}$  of the SW is perpendicular to the external magnetic field  $\mu_0 H_{\text{ext}}$  and excited at  $f = 7$  GHz with  $P_{\text{MW}} = 0$  dBm of microwave power. SWs are detected by the polar magneto-optical Kerr-effect that induces a circular dichroism and subsequent rotation of polarization of the reflected light on the analyzer plane [37, 46].

*Detection characteristics* First, we focus on the properties of the detection mechanisms for SH-SAWs and SWs by our polarization analysis technique. For this, we rotate the analyzer's  $\lambda/2$ -plate. As expected, the linear polarization exhibits a  $\cos^2(\theta)$ -dependence, where  $\theta$  denotes the polarization angle relative to the pure p-polarized state of the incoming light, which is polarized parallel to the  $\lambda/2$ -plates neutral axis and the polarizer axis. This is depicted in Fig. 1 f) and indicated by the normalized light intensity  $I/I(0^\circ)$ . We assess the obtained signal for both the SH-SAW and the SW under variation of the analyzed polarization angle, i.e. of the  $\lambda/2$ -plate angle, relative to its neutral axis. For this, we measure a line scan as depicted in Fig. 1 d) and e) and fit the complex  $S_{21}$  data using [48]:

$$S_{21}(x) = A_0 \cdot e^{-\frac{x}{\xi}} \cdot e^{i(kx - \varphi_0)}. \quad (2)$$

Here,  $A_0$  denotes the detected amplitude and  $\varphi_0$  the phase. The result as a function of the analyzed polarization is shown in Fig. 1 g) for the normalized detected amplitude  $A_0/A_{\text{max}}$  extracted for the Real-part. Remarkably, we find that the SH-SAW is detected most sensitively at an analyzer angle corresponding to maximized intensity modulation, see Fig. 1 f) and is even in symmetry with respect to 0. Concluding, the detected signal dominantly stems from a reflectivity modulation induced by the SAW. Consequently, the incident electric field  $\mathbf{E}_{\text{in}} = (E_{\text{in}}, 0, 0)^T$  is modulated by the SAW phase according to  $\mathbf{E}_{\text{ref}} = ((r_{11} + \Delta r_{11} \cdot \exp(ikx))E_{\text{in}}, 0, 0)^T$ , with  $r_{11}$  being the reflection coefficient and  $\Delta r_{11} \cdot \exp(ikx)$  being the modulation that depends on the phase of the acoustic wave. Selection of the polarization orientation by the polarizer at an angle  $\theta$  on the polarizer axis  $\mathbf{c} = (\cos(\theta), \sin(\theta), 0)^T$  and detection as a DC-voltage  $V_2 \propto [\mathbf{c} \cdot \mathbf{E}_{\text{ref}}]^2$  by the photo diode yields:

$$V_2 \propto [(r_{11} + \Delta r_{11} \cdot \exp(ik_{\text{SAW}}x))E_{\text{in}} \cdot \cos(\theta)]^2. \quad (3)$$

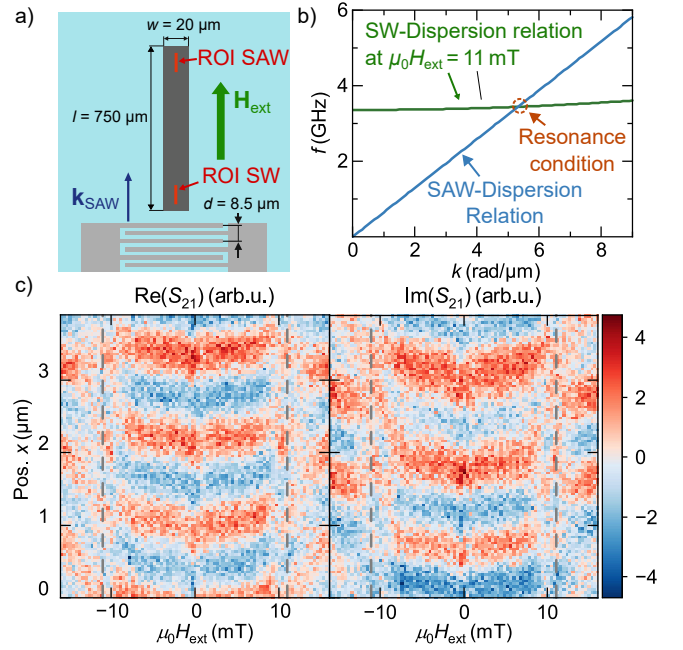


FIG. 2. (a) Shows a sketch of the investigated structure and the measurement geometry. We orient the sample in backward-volume geometry ( $k_{\text{SAW}} \parallel \mu_0 H_{\text{ext}}$ ). The SAW-signal is picked up near the end of the waveguide (marked by ROI SAW). The SW signal shown in Fig. 3 is measured at the start of the  $\text{Co}_{40}\text{Fe}_{40}\text{B}_{20}$ -strip. (b) Shows the derived SAW dispersion relation (blue) and of the SW dispersion relation (green) at  $\mu_0 H_{\text{ext}} = 11$  mT computed using the thin-film approximation derived by Kalinikos-Slavin equation [47]. The SAW frequency ( $f = 3.41$  GHz) and wave vector ( $k = 5.3$  rad/ $\mu\text{m}$ ) excited by our IDT intersect the SW dispersion relation at the external field of  $\mu_0 H_{\text{ext}} = 11$  mT, fulfilling the resonance condition. (c) Shows the measured SAW signal as  $\text{Re}(S_{21})$  and  $\text{Im}(S_{21})$ , detected at "ROI SAW" indicated in (a) at  $0^\circ$  polarization analyzing position, when the SAW is detected most sensitively. At the resonance magnetic field of  $\pm 11$  mT (gray dashed lines) we observe a decrease in SAW amplitude as well as a phase shift, compared to the off-resonant case as a back action of the SW-system on the SAW.

This expression is equivalent to Ref. [49]. From this, it becomes clear that the maximum sensitivity to intensity modulation is obtained at a polarization of  $0^\circ$  with  $180^\circ$  periodicity due to the  $\cos^2(\theta)$ -dependence. Next, considering SW detection, we obtain the maximum signal at analyzer angles that maximize sensitivity to polarization modulation. This aligns with the expectation for the induced circular dichroism by the polar MOKE, which leads to a rotated polarization state on the analyzer plane, depending on the probed SW phase. Notably, we find that the detected real-part amplitude exhibits a sign change when moving from negative to positive analyzer angles, being odd in symmetry with respect to 0, as shown in Fig. 1 g). To understand this, we consider the Kerr-rotated signal in simplified limit given by  $\mathbf{E}_{\text{ref}} = (r_{11}E_{\text{in}}, \Theta_{\text{K},0} \cdot \exp(ikx)r_{12}E_{\text{in}}, 0)^T$ , with  $\Theta_{\text{K},0} \cdot \exp(ikx)$  denoting the polar Kerr angle and  $r_{12}$

the off-diagonal component of the reflectivity tensor. Af-

ter polarization selection and DC voltage detection (see above), we obtain:

$$V_2 \propto [r_{11}E_{\text{in}} \cos(\theta) + \Theta_{\text{K},0} \cdot \exp(ik_{\text{SW}}x)r_{12}E_{\text{in}} \cdot \sin(\theta)]^2 \quad (4)$$

$$\approx r_{11}^2 E_{\text{in}}^2 \cos^2(\theta) + r_{11}r_{21}E_{\text{in}}^2 \Theta_{\text{K}} \exp(ik_{\text{SW}}x) \sin(2\theta). \quad (5)$$

We hereby neglect the quadratic terms  $\Theta_{\text{K}}^2 \approx 0$ . As the first term contains only a constant background, not containing any SW information, we do not consider this part further. The second term includes the polarization modulation. Here  $\text{Re}(V_2^2)$  and  $\text{Im}(V_2^2)$  maximize for  $\sin(2\theta) = \pm 45^\circ$ . Importantly, as  $\sin(2\theta)$  is odd in symmetry at  $0^\circ$ , the detected phase flips by  $180^\circ$  when rotating from  $-\theta$  to  $+\theta$  angles. This flip is depicted in the insets in Fig. 1 g) by the different projection of the GHz-dynamic part of the electric field vector on the polarizer axis. At  $-45^\circ$  one obtains a minimum position after the selection of the polarization orientation on the polarizer, which is denoted by  $\mathbf{c}$ , while on  $+45^\circ$ , one obtains a maximum. The observed behavior is in contrast to the SAW and SW detection using micro-focussed Brillouin light scattering spectroscopy, where SAW and SW signals are in  $90^\circ$  polarization rotation to each other [50]. The polarization dependent footprints allow to discriminate SAW and SW signals. By subtracting the measured  $\text{Re}(S_{21})$  and  $\text{Im}(S_{21})$  at  $-45^\circ$  and  $+45^\circ$ , the SAW signal is effectively diminished, while the SW signal is preserved by exploiting the odd and even symmetry correlations. The corresponding angles are marked in Fig. 1 f).

*Phase-resolved SAW-SW-coupling* Now, we focus on the phase-resolved detection of magnetoelastic SW excitation by SAWs. For this, we place our  $\text{LiTaO}_3/\text{Co}_{40}\text{Fe}_{40}\text{B}_{20}$  sample, oriented with  $k_{\text{SAW}}$  parallel to the external magnetic field  $\mu_0 H_{\text{ext}}$ , commonly called the backward-volume geometry. Thereby, the shear strain component generates an effective magnetoelastic field  $\mu_0 h_{\text{ip}}$  given by:

$$\mu_0 h_{\text{ip}} = -2b_1 \varepsilon_{xy} \cos[2\angle(\mathbf{k}_{\text{SAW}}, \mathbf{M})], \quad (6)$$

where  $b_1$  is the magnetoelastic coupling constant of  $\text{Co}_{40}\text{Fe}_{40}\text{B}_{20}$  and  $\mathbf{M}$  is the magnetization [51]. We choose this configuration, as the SH-SAW  $\varepsilon_{xy}$ -component couples efficiently in the orientation  $\mathbf{k}_{\text{SAW}} \parallel |\mathbf{M}| \mathbf{H}_{\text{ext}}$ , as shown by Küß *et al.* [30, 52]. We excite the SH-SAW at  $f = 3.41$  GHz with  $P_{\text{MW}} = 12$  dBm and first focus on the end of the  $\text{Co}_{40}\text{Fe}_{40}\text{B}_{20}$ -waveguide, marked by "ROI SAW" in Fig. 2 a). As shown in Ref. [36], the total SAW absorption is greatest at the furthest point from the exciting IDT due to the exponential decay of the acoustic wave as it propagates.. We expect resonant SAW-SW coupling when the excited SAWs frequency and wave vector on the SH-SAW dispersion relation match the SW dispersion relation. This is met at an externally applied magnetic

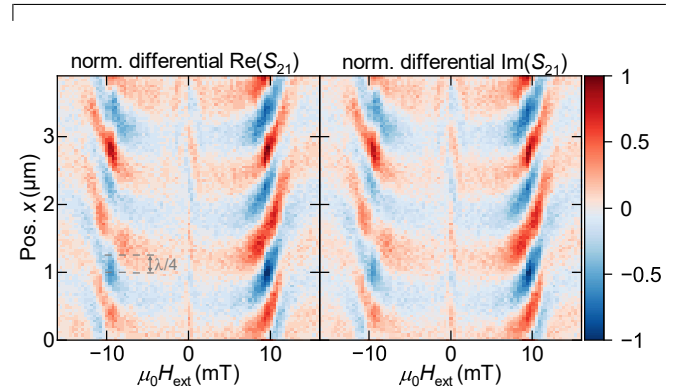


FIG. 3. Spin-wave signal extracted in the ROI SW region, indicated in Fig. 2 a) near the start of the ferromagnetic waveguide. At an external magnetic field of  $\mu_0 H_{\text{ext}} = 11$  mT, the SAW resonantly drives the spin wave. This becomes apparent by the increase in the detected amplitude and the phase difference of  $90^\circ$  of the signal, as marked by the gray dashed lines. The result clearly shows that the SAW drives a coherent SW precession.

field of  $\mu_0 H_{\text{ext}} = \pm 11$  mT, as shown in Fig. 2 b). During the experiment, we rotate the  $\lambda/2$ -plate to  $\theta = 0^\circ$  analyzing position on maximized SAW detection efficiency, and measure linescans for each applied magnetic field. The result is shown in Fig. 2 c) for the obtained  $\text{Re}(S_{21})$  and  $\text{Im}(S_{21})$ . As is evident, at the field of  $\pm 11$  mT the SAW amplitude is strongly decreased and the phase of the acoustic wave is shifted, as one sweeps over the resonance magnetic field. This occurs, as when fulfilling the resonance condition, the acoustic impedance of the material is altered. Consequently, the acoustic absorption and group velocity are modulated, which yields the observed phase shift. This is described by the theory developed by Dreher *et al.* [51] and Küß *et al.* [53] by:

$$\varepsilon_{xy}(x) \propto \exp\left(-\frac{1}{2}\text{Im}(\mathbf{h}^* \bar{\chi} \mathbf{h})x\right), \quad (7)$$

$$\Delta\phi(x) \propto \text{Re}(\mathbf{h}^* \bar{\chi} \mathbf{h})x. \quad (8)$$

Hereby,  $\varepsilon_{xy}(x)$  is the strain and  $\Delta\phi(x)$  the associated phase shift along the propagation direction,  $\mathbf{h}$  is the generated magnetoelastic driving field,  $\bar{\chi}$  is the dynamical Polder susceptibility tensor, and  $x$  denotes the wave's propagated distance over the  $\text{Co}_{40}\text{Fe}_{40}\text{B}_{20}$ . The expression for  $\Delta\phi$  directly follows from the Kramers-Kronig-relations [54, 55].

Finally, we move the detection ROI to the start of the  $\text{Co}_{40}\text{Fe}_{40}\text{B}_{20}$  layer as indicated by ROI SW in Fig. 2 a). As previously described, we measure line-scans as a function of the applied magnetic field. To maximize the obtained response, we repeat the measurement at  $-45^\circ$  and  $+45^\circ$ , and subtract the absolute values of the resulting signal to suppress the SAW contribution and enhance the SW signature. The extracted normalized signal is shown in Fig. 3 for  $\text{Re}(S_{21})$  and  $\text{Im}(S_{21})$ , respectively.

As is evident in Fig. 3 by the strongly increased signal intensity at  $\pm 11$  mT, the resonantly driven SW is detected alongside a  $90^\circ$  positional phase difference of the SW relative to the off-resonantly detected SAW signal. This is analogous to the characteristic  $90^\circ$  phase difference of a driven harmonic oscillator at resonance between the driving force, that is the SAW, and the resonantly driven system, that is the SW at the resonance magnetic field. Profoundly, this measurement shows not only the resonant excitation of the SW but importantly directly demonstrates the coherent driving of the spin-waves precession. Further noticeable is that off-resonantly, the SAW signal does not fully vanish. This is due to the shear strain of the SH-SAW inducing an optical birefringence, which

gives rise to a polarization rotation.

*Summary.* Our measurements demonstrate that, besides SWs, one can detect SAWs using a polarization-intensity analysis experiment. We presented a mean to effectively separate SAW and SW signatures by their distinct polarization footprints. This enables measuring the resonant magnetoelastic coupling between SAWs and SWs, and allows us to directly image the SAW attenuation and phase shift due to the modified acoustic impedance by the SW. Remarkably, we directly showed the resonant and coherent driving of SWs by SAWs, paving the way for the exploitation of magnetoelastic based SW excitation for coherent magnonic applications.

*Acknowledgments.* This work was supported by the European Research Council (ERC) under the European Union’s Horizon Europe research, innovation programme (Consolidator Grant “MAWiCS”, Grant Agreement No. 101044526) and by the Deutsche Forschungsgemeinschaft (DFG, German Research Foundation) by Project No. 492421737 and TRR 173—268565370 (project B01 and B13).

*Data Availability.* The data that support the findings of this article are openly available [56].

- 
- [1] IEEE International Roadmap for Devices and Systems (IRDS) More Moore and Metrology Teams, *IEEE International Roadmap for Devices and Systems (IRDS) 2024 Metrology*, Tech. Rep. (IEEE International Roadmap for Devices and Systems (IRDS), 2024) Feature sizes are expected to reach physical limits where cost and reliability outweigh the benefits of further nanoscale scaling, and physical scaling is no longer the main technology driver for the semiconductor industry.
- [2] P. Barla, V. K. Joshi, and S. Bhat, Spintronic devices: A promising alternative to CMOS devices, *J. Comput. Electron.* **20**, 805 (2021).
- [3] Spintronics for ultra-low-power circuits and systems, *Nat. Rev. Electr. Eng.* **1**, 691 (2024).
- [4] B. Behin-Aein, D. Datta, S. Salahuddin, and S. Datta, Proposal for an all-spin logic device with built-in memory, *Nat. Nanotechnol.* **5**, 266 (2010).
- [5] D. Sander, S. O. Valenzuela, D. Makarov, C. H. Marrows, E. E. Fullerton, P. Fischer, J. McCord, P. Vavassori, S. Mangin, P. Pirro, B. Hillebrands, A. D. Kent, T. Jungwirth, O. Gutfleisch, C. G. Kim, and A. Berger, The 2017 Magnetism Roadmap, *J. Phys. D: Appl. Phys.* **50**, 363001 (2017).
- [6] M. Althammer, Pure spin currents in magnetically ordered insulator/normal metal heterostructures, *J. Phys. D: Appl. Phys.* **51**, 313001 (2018).
- [7] K. Uchida, S. Takahashi, K. Harii, J. Ieda, W. Koshibae, K. Ando, S. Maekawa, and E. Saitoh, Observation of the spin Seebeck effect, *Nat.* **455**, 778 (2008).
- [8] A. Brataas, Y. Tserkovnyak, G. E. W. Bauer, and B. I. Halperin, Spin battery operated by ferromagnetic resonance, *Phys. Rev. B* **66**, 060404 (2002).
- [9] Y. Tserkovnyak, A. Brataas, and G. E. W. Bauer, Spin pumping and magnetization dynamics in metallic multilayers, *Phys. Rev. B* **66**, 224403 (2002).
- [10] L. J. Cornelissen, J. Liu, R. A. Duine, J. B. Yousef, and B. J. van Wees, Long-distance transport of magnon spin information in a magnetic insulator at room temperature, *Nature Physics* **11**, 1022 (2015).
- [11] P. Pirro, V. I. Vasyuchka, A. A. Serga, and B. Hillebrands, Advances in coherent magnonics, *Nat. Rev. Mat.* **6**, 1114 (2021).
- [12] A. N. Mahmoud, F. Vanderveken, C. Adelman, F. Ciubotaru, S. Hamdioui, and S. Cotozana, Multifrequency data parallel spin wave logic gates, *IEEE Trans. Magn.* **57**, 1 (2021).
- [13] H. Y. Yuan, Y. Cao, A. Kamra, R. A. Duine, and P. Yan, Quantum magnonics: When magnon spintronics meets quantum information science, *Phys. Rep.* **965**, 1 (2022).
- [14] S. N. Andrianov and S. A. Moiseev, Magnon qubit and quantum computing on magnon Bose-Einstein condensates, *Phys. Rev. A* **90**, 042303 (2014).
- [15] A. V. Chumak, P. Kabos, M. Wu, C. Abert, C. Adelman, A. O. Adeyeye, J. Åkerman, F. G. Aliev, A. Anane, A. Awad, C. H. Back, A. Barman, G. E. W. Bauer, M. Becherer, E. N. Beginin, V. A. S. V. Bitencourt, Y. M. Blanter, P. Bortolotti, I. Boventer, D. A. Bozhko, S. A. Bunyaev, J. J. Carmiggelt, R. R. Cheenikundil, F. Ciubotaru, S. Cotozana, G. Csaba, O. V. Dobrovolskiy, C. Dubs, M. Elyasi, K. G. Fripp, H. Fulara, I. A. Golovchanskiy, C. Gonzalez-Ballester, P. Graczyk, D. Grundler, P. Gruszecki, G. Gubbiotti, K. Guslienko, A. Haldar, S. Hamdioui, R. Hertel, B. Hillebrands, T. Hioki, A. Houshang, C.-M. Hu, H. Huebl, M. Huth, E. Iacocca, M. B. Jungfleisch, G. N. Kakazei, A. Khitun, R. Khymyn, T. Kikkawa, M. Kläui, O. Klein, J. W. Klos, S. Knauer, S. Koraltan, M. Kostylev, M. Krawczyk, I. N. Krivorotov,

- V. V. Kruglyak, D. Lachance-Quirion, S. Ladak, R. Lebrun, Y. Li, M. Lindner, R. Macédo, S. Mayr, G. A. Melkov, S. Mieszczak, Y. Nakamura, H. T. Nembach, A. A. Nikitin, S. A. Nikitov, V. Novosad, J. A. Otálora, Y. Otani, A. Papp, B. Pigeau, P. Pirro, W. Porod, F. Porrati, H. Qin, B. Rana, T. Reimann, F. Riente, O. Romero-Isart, A. Ross, A. V. Sadovnikov, A. R. Safin, E. Saitoh, G. Schmidt, H. Schultheiss, K. Schultheiss, A. A. Serga, S. Sharma, J. M. Shaw, D. Suess, O. Surzhenko, K. Szulc, T. Taniguchi, M. Urbánek, K. Usami, A. B. Ustinov, T. van der Sar, S. van Dijken, V. I. Vasyuchka, R. Verba, S. V. Kusminskiy, Q. Wang, M. Weides, M. Weiler, S. Wintz, S. P. Wolski, and X. Zhang, Advances in magnetics roadmap on spin-wave computing, *IEEE Trans. Magn.* **58**, 1 (2022).
- [16] D. Breitbach, M. Bechberger, H. Mortada, B. Heinz, R. Verba, Q. Wang, C. Dubs, M. Carpentieri, G. Finocchio, D. Rodrigues, A. A. Hamadeh, and P. Pirro, Allmagnonic neurons for analog artificial neural networks (2025), [arXiv:2509.18321 \[cond-mat.mtrl-sci\]](https://arxiv.org/abs/2509.18321).
- [17] A. A. Serga, A. V. Chumak, and B. Hillebrands, YIG magnonics, *J. Phys. D: Appl. Phys.* **43**, 264002 (2010).
- [18] R. Dreyer, A. F. Schäffer, H. G. Bauer, N. Liebing, J. Berakdar, and G. Woltersdorf, Imaging and phase-locking of non-linear spin waves, *Nat. Comm.* **13**, 4939 (2022).
- [19] D. Breitbach, M. Bechberger, B. Heinz, A. Hamadeh, J. Maskill, K. O. Levchenko, B. Lägél, C. Dubs, Q. Wang, R. Verba, and P. Pirro, Nonlinear erasing of propagating spin-wave pulses in thin-film Ga:YIG, *Appl. Phys. Lett.* **124**, 092405 (2024).
- [20] F. Kohl, B. Heinz, Ádám Papp, R. Erdélyi, G. Csaba, and P. Pirro, Identification and minimization of losses in microscaled spin-wave transducers (2025), [arXiv:2505.08656 \[physics.app-ph\]](https://arxiv.org/abs/2505.08656).
- [21] C. Kittel, Interaction of Spin Waves and Ultrasonic Waves in Ferromagnetic Crystals, *Phys. Rev.* **110**, 836 (1958).
- [22] H. Bömmel and K. Dransfeld, Excitation of Hypersonic Waves by Ferromagnetic Resonance, *Phys. Rev. Lett.* **3**, 83 (1959).
- [23] M. Küß, S. Glamsch, Y. Kunz, A. Hörner, M. Weiler, and M. Albrecht, Giant Surface Acoustic Wave Non-reciprocity with Low Magnetoacoustic Insertion Loss in CoFeB/Ru/CoFeB Synthetic Antiferromagnets, *ACS Appl. Electron. Mater.* **5**, 5103 (2023).
- [24] A. Jander, P. Dhagat, and C. Rivard, Parametric pumping of coherent spin waves by surface acoustic waves, *J. Appl. Phys.* **137**, 073902 (2025).
- [25] M. Geilen, R. Verba, A. Hamadeh, A. Nicoloiu, D. Narducci, A. Dinescu, M. Ender, M. Mohseni, F. Ciubotaru, M. Weiler, A. Müller, B. Hillebrands, C. Adelman, and P. Pirro, Parametric excitation and instabilities of spin waves driven by surface acoustic waves, *Adv. Phys. Res.* **4**, 2400086 (2024).
- [26] Y. Kunz, J. Schüler, F. Ryburn, K. Künstle, M. Schneider, K. Lasinger, Y. Zhang, P. Pirro, J. Gregg, and M. Weiler, Efficient spin-wave excitation by surface acoustic waves in ultralow-damping yttrium iron garnet-zinc oxide heterostructures, *Phys. Rev. Appl.* **24**, 014043 (2025).
- [27] C. Holzmann, M. Küß, S. Glamsch, D. Stein, Y. Kunz, M. Weiler, and M. Albrecht, Polycrystalline YIG Thin Films on a Piezoelectric Substrate for Magnetoacoustic Hybrid Devices, *ACS Appl. Mater. Interfaces* **17**, 58550 (2025).
- [28] K. Künstle, Y. Kunz, T. Moussa, K. Lasinger, K. Yamamoto, P. Pirro, J. F. Gregg, A. Kamra, and M. Weiler, Magnon-polaron control in a surface magnetoacoustic wave resonator, *Nat. Comm.* **16**, 10116 (2025).
- [29] Y. Hwang, J. Puebla, K. Kondou, C. Gonzalez-Ballester, H. Isshiki, C. S. Muñoz, L. Liao, F. Chen, W. Luo, S. Maekawa, and Y. Otani, Strongly Coupled Spin Waves and Surface Acoustic Waves at Room Temperature, *Phys. Rev. Lett* **132**, 056704 (2024).
- [30] M. Küß, M. Heigl, L. Flacke, A. Hefe, A. Hörner, M. Weiler, M. Albrecht, and A. Wixforth, Symmetry of the Magnetoelastic Interaction of Rayleigh and Shear Horizontal Magnetoacoustic Waves in Nickel Thin Films on LiTaO<sub>3</sub>, *Phys. Rev. Appl.* **15**, 034046 (2021).
- [31] M. Weiler, L. Dreher, C. Heeg, H. Huebl, R. Gross, M. S. Brandt, and S. T. B. Goennenwein, Elastically Driven Ferromagnetic Resonance in Nickel Thin Films, *Phys. Rev. Lett* **106**, 117601 (2011).
- [32] M. Weiler, H. Huebl, F. S. Goerg, F. D. Czeschka, R. Gross, and S. T. B. Goennenwein, Spin Pumping with Coherent Elastic Waves, *Phys. Rev. Lett* **108**, 176601 (2012).
- [33] M. Kraimia, P. Kuszewski, J.-Y. Duquesne, A. Lemaître, F. Margailan, C. Gourdon, and L. Thevenard, Time- and space-resolved nonlinear magnetoacoustic dynamics, *Phys. Rev. B* **101**, 144425 (2020).
- [34] B. Casals, N. Statuto, M. Foerster, A. Hernández-Mínguez, R. Cicheler, P. Manshausen, A. Mandziak, L. Aballe, J. M. Hernández, and F. Macià, Generation and Imaging of Magnetoacoustic Waves over Millimeter Distances, *Phys. Rev. Lett.* **124**, 137202 (2020).
- [35] T. Sebastian, K. Schultheiss, B. Obry, B. Hillebrands, and H. Schultheiss, Micro-focused Brillouin light scattering: Imaging spin waves at the nanoscale, *Front. Phys.* **3**, 10.3389/fphy.2015.00035 (2015).
- [36] Y. Kunz, M. Küß, M. Schneider, M. Geilen, P. Pirro, M. Albrecht, and M. Weiler, Coherent surface acoustic wave-spin wave interactions detected by micro-focused Brillouin light scattering spectroscopy, *Appl. Phys. Lett.* **124**, 152403 (2024).
- [37] L. Liensberger, L. Flacke, D. Rogerson, M. Althammer, R. Gross, and M. Weiler, Spin-Wave Propagation in metallic Co<sub>25</sub>Fe<sub>75</sub> Films Determined by Microfocused Frequency-Resolved Magneto-Optic Kerr Effect, *IEEE Magn. Lett.* **10**, 1 (2019).
- [38] A. A. Serga, T. Schneider, B. Hillebrands, S. O. Demokritov, and M. P. Kostylev, Phase-sensitive Brillouin light scattering spectroscopy from spin-wave packets, *Appl. Phys. Lett.* **89**, 063506 (2006).
- [39] O. Wojewoda, M. Hrtoň, M. Dhankhar, J. Krčma, K. Davidková, J. Klíma, J. Holobrádek, F. Ligmajer, T. Šíkola, and M. Urbánek, Phase-resolved optical characterization of nanoscale spin waves, *Appl. Phys. Lett.* **122**, 202405 (2023).
- [40] See Supplemental Material at [URL will be inserted by publisher] for details on the sample fabrication.
- [41] C. Thomsen, H. T. Grahn, H. J. Maris, and J. Tauc, Surface generation and detection of phonons by picosecond light pulses, *Phys. Rev. B* **34**, 4129 (1986).
- [42] S. H. Wemple and M. DiDomenico, Theory of the Elastooptic Effect in Nonmetallic Crystals, *Phys. Rev. B* **1**, 193 (1970).

- [43] O. B. Wright, O. Matsuda, and Y. Sugawara, Real Time Imaging of Surface Acoustic Waves on Crystals and Microstructures, *Jpn. J. Appl. Phys.* **44**, 4292 (2005).
- [44] O. Matsuda and O. B. Wright, Reflection and transmission of light in multilayers perturbed by picosecond strain pulse propagation, *JOSA B* **19**, 3028 (2002).
- [45] Q. Xie, S. Mezil, P. H. Otsuka, M. Tomoda, J. Laurent, O. Matsuda, Z. Shen, and O. B. Wright, Imaging gigahertz zero-group-velocity Lamb waves, *Nat. Comm.* **10**, 2228 (2019).
- [46] J. Hamrle, J. Pištora, B. Hillebrands, B. Lenk, and M. Münzenberg, Analytical expression of the magneto-optical Kerr effect and Brillouin light scattering intensity arising from dynamic magnetization, *J. Phys. D: Appl. Phys.* **43**, 325004 (2010).
- [47] B. A. Kalinikos and A. N. Slavin, Theory of dipole-exchange spin wave spectrum for ferromagnetic films with mixed exchange boundary conditions, *J. Phys. C: Solid State Phys.* **19**, 7013 (1986).
- [48] T. Sebastian, Y. Ohdaira, T. Kubota, P. Pirro, T. Brächer, K. Vogt, A. A. Serga, H. Naganuma, M. Oogane, Y. Ando, and B. Hillebrands, Low-damping spin-wave propagation in a micro-structured Co<sub>2</sub>Mn<sub>0.6</sub>Fe<sub>0.4</sub>Si Heusler waveguide, *Appl. Phys. Lett.* **100**, 112402 (2012).
- [49] P. V. Santos, Acoustic field mapping on GaAs using microscopic reflectance and reflectance anisotropy, *Appl. Phys. Lett.* **74**, 4002 (1999).
- [50] M. Geilen, A. Nicoloiu, D. Narducci, M. Mohseni, M. Bechberger, M. Ender, F. Ciubotaru, A. Müller, B. Hillebrands, C. Adelman, and P. Pirro, Fully Resonant Magneto-elastic Spin-wave Excitation by Surface Acoustic Waves under Conservation of Energy and Linear Momentum, *Appl. Phys. Lett.* **120**, 242404 (2022), 2106.14705 [cond-mat].
- [51] L. Dreher, M. Weiler, M. Pernpeintner, H. Huebl, R. Gross, M. Brandt, S. Goennenwein, Surface acoustic wave-driven ferromagnetic resonance in nickel thin films: Theory and experiment, *Phys. Rev. B Condens. Matter* **86**, 5 (2012).
- [52] M. Küß, M. Albrecht, and M. Weiler, Chiral Magnetoacoustics, *Front. Phys.* **10**, 981257 (2022).
- [53] M. Küß, M. Heigl, L. Flacke, A. Hörner, M. Weiler, M. Albrecht, and A. Wixforth, Nonreciprocal Dzyaloshinskii–Moriya Magnetoacoustic Waves, *Phys. Rev. Lett* **125**, 217203 (2020).
- [54] H. A. Kramers, La diffusion de la lumière par les atomes, in *Atti del Congresso Internazionale dei Fisici*, Vol. 2 (Como, Italy, 1927) pp. 545–557.
- [55] R. d. L. Kronig, On the Theory of Dispersion of X-Rays, *JOSA* **12**, 547 (1926).
- [56] 10.5281/zenodo.18880206.